Article

Logical Optimization of Metal−Organic Frameworks for Photocatalytic Degradation of Organic Pollutants in Water via Box−Behnken Design

Iqra Afzal, Toheed Akhter,* Sadaf Ul Hassan, Ho Kyung Lee, Shumaila Razzaque, Asif Mahmood, Waheed Al-Masry, Hansol Lee, and Chan Ho Park*
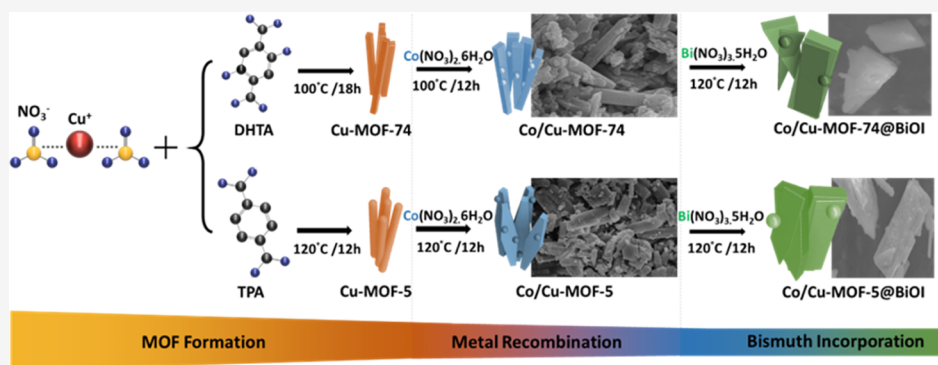
Read Online

ACCESS | Metrics & More | Article Recommendations | Supporting Information

ABSTRACT: Cobalt/copper-based bimetallic metal−organic frameworks (Co/Cu-MOFs) are synthesized using two organic ligands in the presented research work. Subsequent incorporation of bismuth oxyiodide (BiOI) into the MOFs via a hydrothermal approach formed composite materials (Co/Cu-MOFs@BiOI) that exhibit an efficient photocatalytic activity. The synthesized materials were thoroughly characterized by using X-ray diffraction, Fourier transform infrared, and scanning electron microscopy techniques. Co/Cu-MOF @BiOI was employed as a novel photocatalyst for the degradation of cationic methylene blue (MB) dye in aqueous solution under visible light. The combination of Co/Cu-MOFs with BiOI significantly enhanced the photocatalytic degradation efficiency of MB relative to that of bimetallic MOFs (Co/Cu-MOFs) owing to increased visible light absorption and reduced charge-carrier recombination. A Box−Behnken design (BBD) statistical study is employed in conjunction with response surface methodology (RSM) to optimize the dye degradation process. The BBD-RSM methodology successfully identified the optimal dye degradation conditions, including an initial dye concentration of 6 ppm, irradiation time of 120 min, and catalyst dosage of 0.14 g L^{-1}. Furthermore, the predicted coefficient of regression (R^2) value under these optimal conditions using BBD-RSM was 99%, indicating a strong correlation between the prediction and experimental observation. These results demonstrate the strong potential of the Co/Cu-MOF @BiOI composites as efficient photocatalysts for the removal of organic dyes.

KEYWORDS: photocatalysis, MOFs, bimetallic composites, BiOI, dye degradation, Box−Behnken design

1. INTRODUCTION

Water contamination by industrial pigments from dye manufacturing and consumption industries, including fabric inks, pigments for display applications, and cosmetic dyes, is a major global issue that significantly impacts human life and social development.[1] At least 10% of the approximately 800,000 tons of dyes and pigments generated annually worldwide enter into the environment.[2] A dye concentration of less than 1 ppm can have severe negative impacts on the environment, including reduced photosynthetic activity, reduced sunlight penetration, lowered dissolved oxygen concentration, and damage to aquatic ecosystems.[3] Methylene blue (MB) is a representative organic cationic dye. This sulfur-containing heterocyclic aromatic compound is frequently used

across numerous industries, including the leather, paper, textile, pharmaceutical, and cosmetic industries.[4] Inadequate containment measures lead to the discharge of organic dyes and their precursors, posing a significant health hazard to both humans and wildlife due to their elevated levels of toxicity and carcinogenic properties.[1] Methods and technologies for the

removal of organic dyes from aqueous solutions are urgently required to overcome such environmental issues. Existing methods for this purpose include physical, biological, and chemical processes such as activated carbon adsorption,[5] coagulation and flocculation,[6] ultrafiltration membranes,[7] ozonation,[8] ultraviolet radiation,[9] chemical recovery, sedimentation,[10] and advanced oxidation processes (AOPs).[11] AOPs involve oxygen species (ROS), including superoxide or hydroxyl radicals, produced by the activation of a suitable ROS precursor by ultraviolet light. ROS oxidize and degrade various organic substances,[12] enabling the photocatalytic decomposition of organic dyes by renewable solar light in the presence of a suitable catalyst. This is considered one of the most environmentally friendly methods of converting hazardous materials into nontoxic compounds without causing secondary pollution.[13]

Among numerous photocatalytic materials, the photocatalytic performance of ZnO and TiO$_2$ semiconductors in the elimination of organic pollutants from industrial effluents has recently attracted significant attention.[14] These photocatalysts are only activated by ultraviolet light in the solar region owing to their high band gap, which, along with other drawbacks such as low solar energy utilization, rapid charge-carrier recombination, and facile agglomeration, limits their implementation.[15] The development of new materials with a small band gap, high catalytic efficiency, and large capacity for absorbing visible light is therefore required. Bismuth oxyhalides (Cl, Br, and I) are promising next-generation photocatalysts owing to their excellent photocatalytic activity under visible light, high stability, diverse band structure, nontoxicity, cost-effectiveness, and well-defined layered architecture denoted as X−Bi−O−X.[16] Among other bismuth oxyhalides, bismuth oxyiodide (BiOI) has the lowest band gap (1.7−1.9 eV) and has demonstrated remarkable photocatalytic activity;[17] however, BiOI suffers from rapid charge-carrier recombination that limits its utility as a photocatalyst. Numerous recent studies have sought to prevent this photoexcited charge-carrier recombination by developing BiOI-based heterostructures,[18] many of which, including 3D hollow magnetic (Fe$_3$O$_4$/BiOI),[19] bismuth oxyiodide coupled with titanium dioxide (BiOI/TiO$_2$),[20] and loading of reduced graphene oxide on BiOI (rGO@BiOI), have previously demonstrated high photocatalytic efficiency in the removal of organic contaminants.[17]

MOFs have demonstrated strong potential as catalysts owing to strong coordination of the metal with the ligand, appropriate porosity, and increased surface area. Numerous single-metal MOFs including [Ni$_2$(C$_{10}$H$_8$N$_2$)$_2$][C$_{12}$H$_8$O(COO)$_2$]2H$_2$O, [Co$_2$(C$_{10}$H$_8$N$_2$)], and [C$_{12}$H$_8$O(COO)$_2$]$_2$[21] have shown enhanced catalytic efficiency in the degradation of organic dyes. Bimetallic MOFs, in which two metals are coordinated with an organic linker, exhibit superior photocatalytic performance than single-metal MOFs, which is attributed to the synergistic interaction between the metal constituents.[22] Additionally, bimetallic MOFs offer increased flexibility in designing catalyst structures by simply adjusting the metal ratio.[23]

Several studies investigated the ability of bimetallic MOFs to degrade organic pollutants. For instance, methyl orange and methyl blue can be degraded by a bimetallic Fe/Ni-MOF (FeNiX-TPA),[24] while tetracycline hydrochloride can be oxidized using a bimetallic Fe/In MOF[25] and catalytic ozonation of atrazine can be achieved using Co/Ni-MOF-

74.[26] Garcia et al. used MOF-5 as an effective photocatalyst for the decomposition of phenol.[27] Natarajan et al. developed a series of photocatalytic MOFs containing nickel, zinc, and cobalt for the degradation of organic dyes,[28] while Jing et al. used photoactive ZIF-8 in the degradation of methylene blue;[29] however, the limited visible-light absorption of bimetallic MOFs inhibits their photocatalytic efficiency. The combination of two photocatalysts to form heterostructures that can efficiently photodegrade organic contaminants is key to improving the efficiency of MOF-based photocatalysts.[30] In this regard, numerous heterostructures, including BiOI with MOF, rGO, and g-C$_3$N$_4$, have been developed to increase the surface area, boost visible-light absorption, and prevent the recombination of photoexcited charge carriers.[31] In this regard, we explored the application of MOFs in combination with BiOI (MOF@BiOI) as composite materials to enhance the photocatalytic performance of BiOI in our previous study.[32] Specifically, Co/Ni-MOF@BiOI nanocomposites were synthesized, demonstrating a photocatalytic efficiency of approximately 99% for the degradation of MB under visible light. However, a systematic research methodology has not been presented for future research on numerous combinations of metal elements, organic ligands, and heterogeneous catalysts, such as Box−Behnken design (BBD) in conjunction with response surface methodology (RSM).

In this work, Co-doped Cu-MOFs were prepared by using DHTA as an organic linker. BiOI was incorporated into the prepared Co/Cu-DHTA MOFs to obtain the Co/Cu-DHTA@BIOI heterostructures. To assess how DHTA influences the characteristics of these heterostructures, another set of heterostructures was prepared in which terephthalic acid was used as an organic linker rather than DHTA. The structures of the prepared materials were evaluated by using XRD, SEM, and EDX analyses. The photocatalytic performance of these heterostructures was examined by analyzing their ability to degrade MB under direct solar light irradiation. The photocatalytic removal of MB using BiOI-based bimetallic MOFs depends on several parameters, making it difficult to perform and manage these experiments; therefore, a robust approach is required to avoid improper and inconsistent results.[33] Statistical modeling and experimental design techniques have been suggested for the analysis and optimization of such experiments, which involve several variables.[34] Response surface methodology (RSM) is among the most effective experimental design strategies in developing a formulation with the maximum number of variables while performing the minimum number of tests.[33] RSM with a Box−Behnken design (BBD) was therefore utilized, which facilitated us to enhance and optimize the photocatalyst performance of the prepared materials efficiently, ensuring a systematic and reliable exploration of the factors influencing the photocatalytic efficiency.

2. EXPERIMENTAL SECTION

2.1. Materials. 2,5-Dihydroxy terephthalic acid (DHTA) (98%), terephthalic acid (TPA) (99%), Cu(NO$_3$)$_2$·3H$_2$O, (99.5%), Co(NO$_3$)$_2$·6H$_2$O (97%), Bi(NO$_3$)$_3$·5H$_2$O (71%), ethylene glycol [(EG) 99%], potassium iodide [(KI) 99%], deionized water, solvents, and methylene blue (H$_{16}$H$_{18}$ClN$_3$S) (97%) were acquired from Sigma-Aldrich and employed without additional purification.

2.2. Synthesis of Cu-DHTA MOF (PC-1) and Bimetallic Co/Cu-DHTA (PC-2). PC-1 was synthesized by dissolving

DHTA (7.41 mmol) and copper nitrate trihydrate (3.98 mmol) in DMF (25 mL) with constant stirring following an established method.[35] After complete dissolution of the reagents, deionized water (6.5 mL) was added to obtain a clear, green solution. This mixture was introduced into a sealed autoclave lined with Teflon and subjected to heating at 100 °C for an 18 h duration, resulting in the formation of needle-shaped crystals. The crystals were separated by centrifugation and washed with DMF. The product was then immersed in methanol for 24 h before, and then the solvent was replaced once with a fresh batch of the same solvent. The product was obtained through filtration and subsequently subjected to vacuum drying at 70 °C. PC-2 was synthesized using the same procedure, except that cobalt nitrate hexahydrate (3.7 mmol) was added along with copper nitrate trihydrate and DHTA.

2.3. Synthesis of Cu-TPA MOF (PC-3) and Bimetallic Co/Cu-TPA MOF (PC-4).
PC-3 and PC-4 were prepared by a typical hydrothermal method in which copper nitrate trihydrate (0.8 mmol) was dissolved in distilled water (16 mL). Separately, a solution of TPA (1.2 mmol) in 5 mL of DMF was prepared, and this solution was subsequently combined with the copper nitrate trihydrate solution. After 30 min of stirring, the mixture was transferred to an autoclave and heated at 150 °C for 12 h in an oven. Subsequently, the reaction mixture was cooled to afford precipitates of the product, which were filtered and rinsed with absolute ethanol and distilled water. Finally, the solid product was dried overnight at 120 °C. The same method was used to synthesize PC-4, with the addition of cobalt nitrate hexahydrate (2.11 mmol) alongside copper nitrate trihydrate and TPA.

2.4. Synthesis of BiOI-Reinforced Heterostructures of PC-2 and PC-3.
To enhance the photocatalytic activity, the BiOI-reinforced heterostructures of PC-2 and PC-3 were prepared following an established procedure, with slight modifications.[17] $Bi(NO_3)_3 \cdot 5H_2O$ (9.9 mmol) and KI (6.6 mmol) were dissolved separately in EG (40 mL). Both solutions were stirred for 30 min to obtain clear solutions before a calculated amount of the required bimetallic MOF was added to the BiOI solution and the KI solution was added dropwise into this solution. This reaction mixture was stirred at approximately 30 °C for 1 h to attain a brown suspension, which was heated at 120 °C for a further 12 h in a closed oven using a Teflon-lined autoclave. The resulting precipitate was filtered, washed repeatedly with distilled water, and dried overnight.

Four different heterostructures were prepared by using this method: Co/Cu-DHTA@BiOI-10 (denoted PC-5, with 10% BiOI by weight), Co/Cu-DHTA@BiOI-15 (denoted PC-6, with 15% BiOI by weight), Co/Cu-TPA@BiOI-10 (denoted PC-7, with 10% BiOI by weight), and Co/Cu-TPA@BiOI-15 (denoted PC-8, with 15% BiOI by weight). Table 1 lists all photocatalysts and their labels, while the synthesis of all of the photocatalysts is illustrated in Figure 1.

2.5. Characterization of Materials.
The phases and crystalline structure of the samples prepared in this study were analyzed by using X-ray diffraction (XRD) with a Cu Kα radiation source (wavelength λ = 0.15406 nm) in the 2θ range of 10−80°, employing a Bruker D2 instrument. Sample morphologies were examined by using field emission scanning electron microscopy (FE-SEM; Nova NanoSEM 450). Fourier transform infrared spectroscopy (FTIR, Bruker α Platinum ATR) with standard KBr beam splitters in the range of 4000−400 cm^{-1} was used to characterize the photocatalysts. The

Table 1. The List of Synthesized Photocatalysts

Notation	Sample Description	Notes
PC-1	Cu-DHTA MOF	Cu-MOF-74
PC-2	Co/Cu-DHTA MOF	Co-doped Cu-MOF-74
PC-3	Cu-TPA MOF	Cu-MOF-5
PC-4	Co/Cu-TPA MOF	Co-doped Cu-MOF-5
PC-5	Co/Cu-DHTA@BiOI-10%	-
PC-6	Co/Cu-DHTA@BiOI-15%	-
PC-7	Co/Cu-TPA@BiOI-10%	-
PC-8	Co/Cu-TPA@BiOI-15%	-

photoluminescence (PL) spectra of the photocatalysts were measured by an Edinburgh FL/FS900 spectrophotometer using a 380 nm excitation wavelength.

2.6. Photocatalytic Activity.
The photocatalytic performance of the synthesized catalysts (PC1-PC8) was assessed by investigating the photocatalytic degradation of MB under direct sunlight in the presence of the catalysts. MB solutions of various concentrations and the required amounts of photocatalyst were added to closed transparent glass containers and exposed to direct sunlight. During irradiation, the temperature was measured in the range of 30−35 °C, the intensity of sunlight was 240 W/m^2, and the relative humidity was 35%. Prior to light irradiation, the MB solution was stored in the dark for 30 min with constant stirring to reach an adsorption−desorption equilibrium. The samples were then irradiated for specific periods of 0, 60, 120, 180, and 240 min, and the reduction in the MB concentration was determined by UV−visible spectroscopic analysis of each sample. Each sample was analyzed in triplicate to measure the average catalytic efficiency. The MB removal efficiency of each catalyst was calculated using eq 1.[36]

$$\%MB\ degradation = \frac{(C_o - C)}{C} \times 100\%$$
(1)

Here, C_o represents the initial concentration of MB and C denotes its final concentration. The photocatalytic performance of each catalyst was evaluated in terms of the irradiation time, amount of catalyst, and MB concentration using response surface methodology to study the relationships between different variables using the BBD.

3. RESULTS AND DISCUSSION

3.1. FTIR Spectroscopic Analysis.
Figure 2a,b shows the FTIR spectra for the single-metal and bimetallic MOF samples (PC-1 to PC-4). The absorption band at approximately 3400 cm^{-1} in the spectra of PC-1 and PC-2 is attributed to the stretching vibrations of hydroxyl groups at positions 2 and 5 of the aromatic ring of the organic linker (Figure 2b). This absorption band was absent from the spectra of PC-3 and PC-4 because the organic linker in these catalysts does not contain hydroxyl groups. The absorption band of the carbonyl group in the spectra of all samples shifted to a much lower frequency (approximately 1650 cm^{-1}) than its typical absorption frequency of 1710 cm^{-1}, owing to the deprotonation of carboxylic acid groups; however, a partially uncoordinated carboxylic group (red shadow) is also confirmed in the spectra.[37] The wide band at 1095 cm^{-1} in the spectrum of PC-1 is attributed to stretching vibrations of the C−O bonds. This band was not observed in the spectrum of PC-2, as it shifted to peaks at different positions, such as another C−O peak at 1192 cm^{-1}, contributing to the coordination of organic linker with
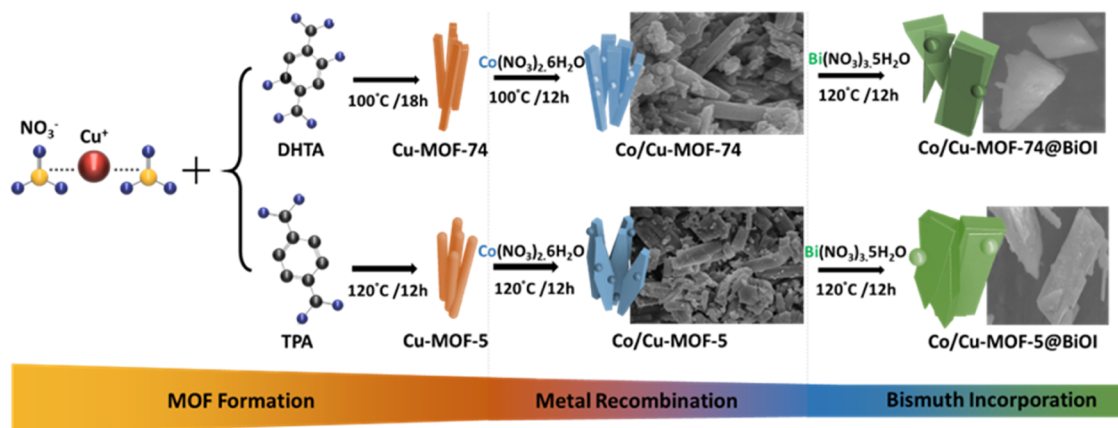
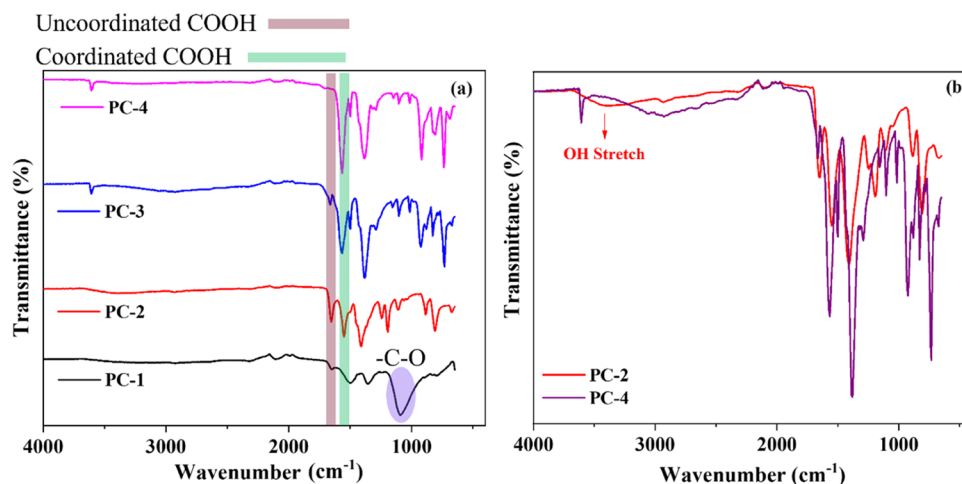**Figure 1.** Synthesis of Co/Cu-MOF@BiOI composite.

Figure 2. (a) FT-IR spectra of photocatalysts (PC-1, PC-2, PC-3, and PC-4). (b) Comparison of FT-IR spectra of PC-2 and PC-4.
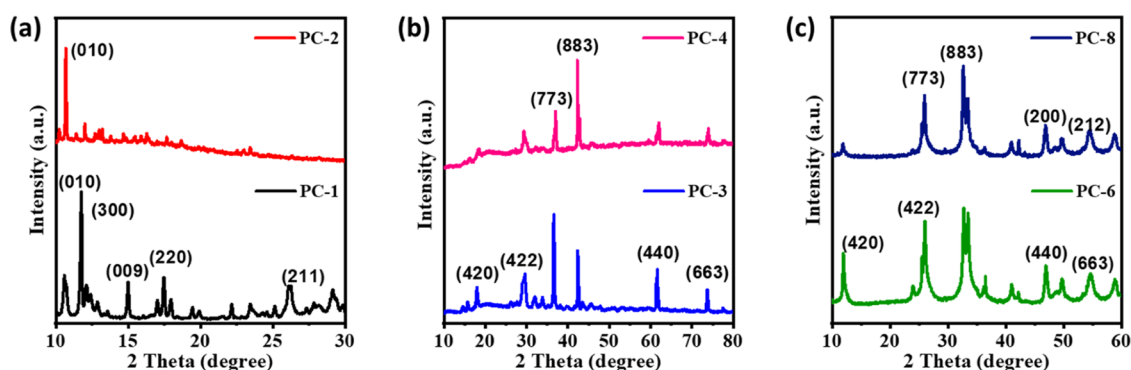

Figure 3. XRD patterns of (a) PC-1 and PC-2, (b) PC-3 and PC-4, and (c) PC-6 and PC-8.

two metals.[38] Similarly, the absorption bands below 800 cm^{-1} in all spectra are attributed to Cu−O and Co−O stretching vibrations. The obtained spectroscopic data are in good agreement with previously published data.[39]

3.2. XRD Analysis. Figure 3a−c shows the XRD patterns of the MOFs (PC1-PC4) and their composites (PC-6 and PC-8, which were reinforced with 15 wt % BiOI). PC-1 exhibited diffraction peaks at specific 2θ angles, including 10.50, 47.9, 13.26, 16.77, 26.0, and 29.0°, corresponding to the crystal planes (010), (300), (009), (220), and (211), respectively, as evident in the XRD pattern. This XRD pattern is in good agreement with that of Cu-MOF-74,[39] demonstrating the

successful preparation of the material without impurities. In the XRD pattern of PC-2 (Figure 3a), the diffraction peak at $2\theta = 10.60°$ is much more intense than that in the pattern of PC-1. Moreover, the XRD pattern of PC-2 differs considerably from that of PC-1 because PC-2 has a different structural framework owing to the incorporation of larger Co^{2+} with smaller Cu^{2+}. In addition, the diffraction peaks in the pattern of PC-2 shifted to higher 2θ values, indicating that the Co:Cu ratio influenced the crystal phase of the bimetallic MOF. The XRD patterns of PC-3 and PC-4 show peaks at $2\theta = 14.55$, 15.73, 17.90, 29.54, 36.53, 42.30, and 61.30° (Figure 3b), which can be indexed at the (222), (333), (420), (422), (773),
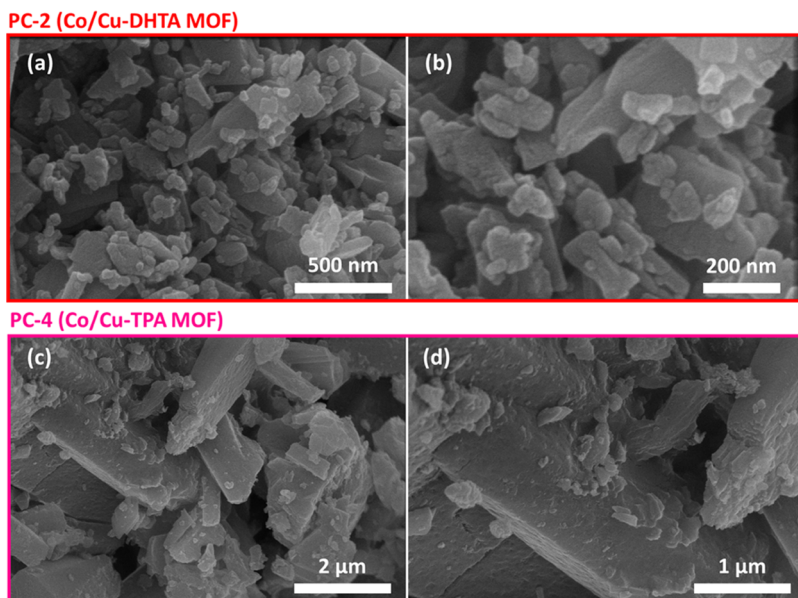
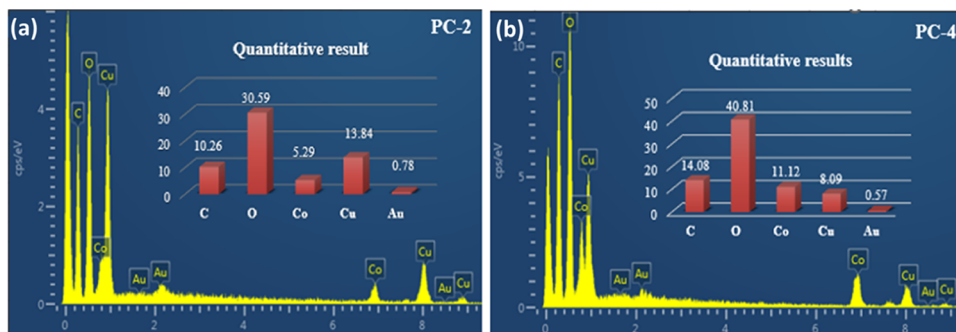**Figure 4.** SEM images of (a, b) PC-2 and (c, d) PC-4.

Figure 5. EDX analysis of (a) PC-2 and (b) PC-4.

(883), (440), and (533) crystal planes, respectively. This data is in agreement with previous studies.[35,40] The XRD patterns of PC-6 and PC-8 (Figure 3c) show four major peaks at $2\theta =$ 29.90, 35.27, 46.96, and 54.54°, which were assigned to the (102), (110), (200), and (212) crystal planes.

3.3. SEM. SEM analysis was used to examine the morphologies of the synthesized materials. SEM images of PC-2 and PC-4 (Figure 4a−d) show the regular and crystalline nature of PC-2, in which the crystals have a rod-like structure (Figure 4a,b), and the rod-like crystals of PC-4 (Figure 4c,d), with a pentagonal shape and expanded diameters. The difference in the shapes and sizes of the crystals of PC-2 and PC-4 was attributed to the differences in the structures of the organic linkers of the materials. These SEM results are in agreement with previously published reports.[30] Similarly, Figure 5 (I, II) shows the EDX spectra of PC-2 and PC-4, which confirm the presence of carbon, oxygen, copper, and cobalt.

Similarly, SEM images of PC-6 and PC-8 (Figure 6a,b) show the crystalline nature of both materials, with cubic and rod-like crystals in PC-6 and PC-8, respectively, owing to differences in the organic linkers of both samples. The morphologies of PC-6 and PC-8 clearly differ from those of PC-2 and PC-4 (Figure 4). This was attributed to the incorporation of BiOI into the MOF, which enhanced the photocatalytic activity of these catalysts for MB degradation.[39] The EDX spectra of PC-6 and

PC-8 clearly show the presence of Bi, Co, and Cu (Figure 7), which confirms the successful incorporation of BiOI into the MOF and the formation of PC-6 and PC-8 heterostructures.

3.4. Optimization and Evaluation of Photocatalytic Activity Using Response Surface Methodology. RSM was used to optimize the study of the correlation between multiple independent variables and the values of important parameters via the BBD. The Design-Expert (version 13) model was used to analyze the effectiveness and accuracy of the experimental data. This approach is frequently used to examine various phenomena including photocatalytic decomposition. All experiments in our study were designed using the RSM, which reduces both the cost and the duration of the procedure. The influence of three key parameters on MB degradation was examined, viz., the MB concentration (A), irradiation time (B), and catalyst dosage (C). A 17-trial study was performed, in which each experiment was performed in duplicate, for the statistical modeling of the experiments, and each independent variable was measured at two levels, low (−1) and high (+1). Table 2 lists the experimental ranges of the different independent variables.

3.5. Dye Degradation and Model Fitting. Prior to the BBD-RSM studies, the catalytic activity of each photocatalyst (PC1-PC8) was evaluated by examining the degradation of MB in the presence of each catalyst under solar-light irradiation (Figure 8). MB was stable in sunlight in the
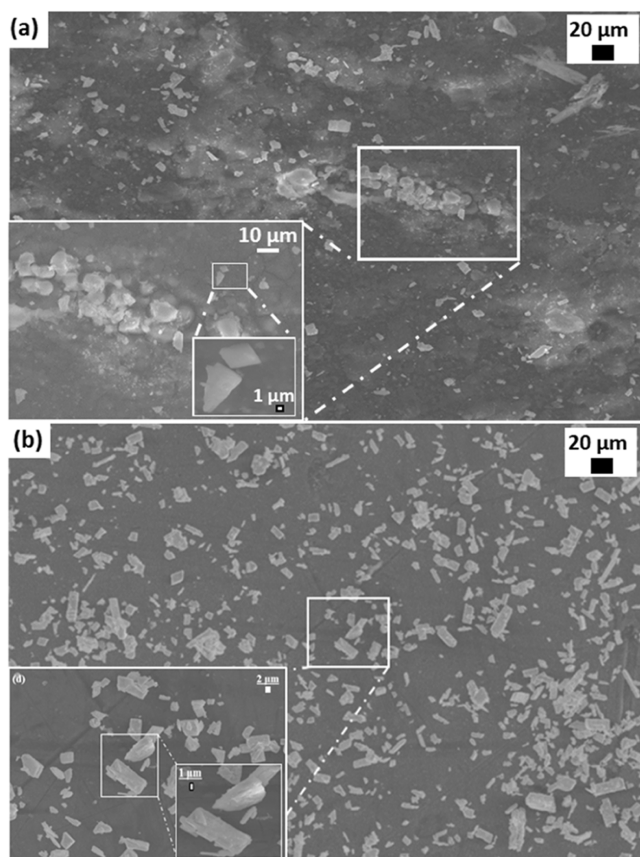
Figure 6. SEM micrographs of (a) PC-6 and (b) PC-8.

Table 2. Experimental Design Using the Box–Behnken Method: Variable Settings and Levels

variables	units	ranges of levels	
		−1 (maximum)	+1 (minimum)
concentration (A)	ppm	6.5 ppm	10 ppm
degradation time (B)	min	60 min	120 min
amount of catalyst (C)	g	0.08 g	0.2 g

absence of the photocatalyst with a negligible degradation (Figure 8a, blank). The PC1-PC4 photocatalysts removed 63–79% MB from the aqueous solution after irradiation for 240 min (Figure 8b,c). The relatively low photocatalytic activity of the single-metal and bimetal MOFs is a consequence of their low visible light absorption (refer to Figure S1 for the UV–

visible spectra of the prepared materials), and MB was mainly removed from the aqueous solution via adsorption on the surface of the photocatalysts. The single-metal MOFs (PC-1 and PC-3) showed lower photocatalytic activity than the bimetallic MOFs (PC-2 and PC-4), likely owing to the incorporation of Co^{2+} ions into the Cu-MOF. Metal dopants are known to serve as mediators between the metal and the organic linker, thereby improving photocatalytic activity.[45] The photocatalytic activities of PC-5, PC-6, PC-7, and PC-8 were significantly higher than those of the MOFs, achieving 97, 99.5, 97.5, and 98.8% MB degradation, respectively, in aqueous solution (Figure 8c,d). The enhanced photocatalytic performance of the composites (PC-5, PC-6, PC-7, and PC8) can be ascribed to the incorporation of BiOI into the MOF matrix. The incorporation of BiOI shifts the light absorption band toward the visible light wavelength, which facilitates the photoinduced excitation of charges.[41] In Figure S1a, the UV–vis profile of PC-6 showed higher solar light absorption in the visible wavelength range compared to PC-1 and PC-2. Regardless of the organic ligand in the MOF, TPA-based photocatalytic MOFs also showed a similar trend (Figure S1b). The enhancement of light absorption in the visible light range is an efficient way to collect light energy since the spectral irradiance of solar light is largely overlapped with the visible range, as shown in Figure S1a,b. Moreover, these characteristics were supported by the results from PL emission quenching measurements. The degrees of PL quenching for BiOI, MOFs, and MOF@BiOI heterostructures were compared by excitation at 380 nm (Figure S2). PL quenching
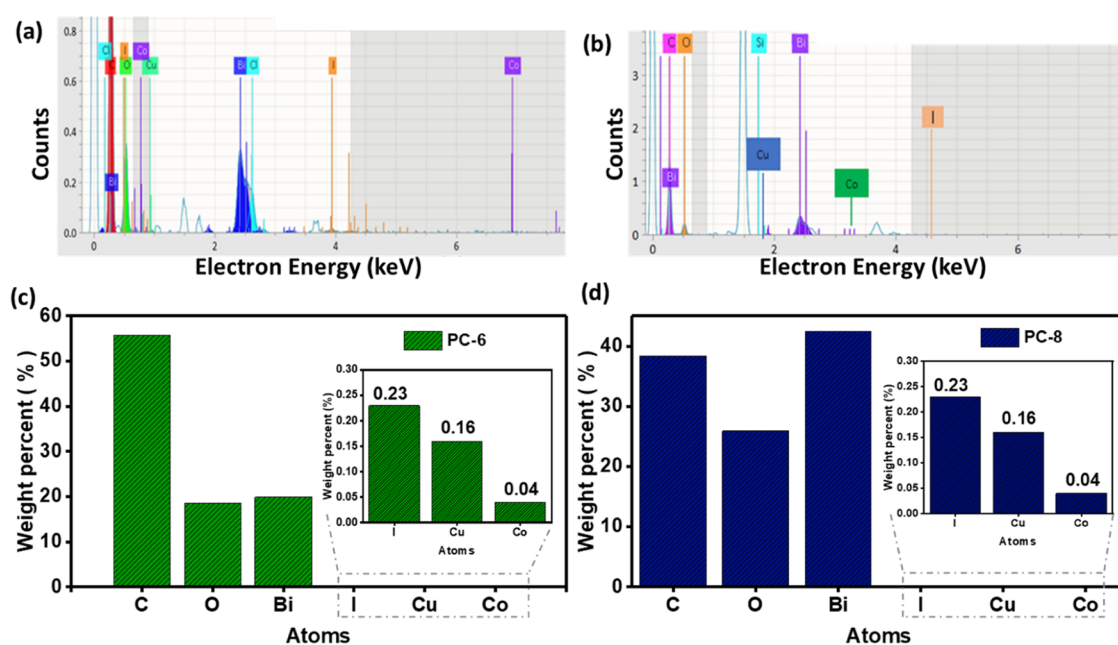

Figure 7. EDX/EDS spectra of (a) PC-6 and (b) PC-8. Elemental analysis of (c) PC-6 and (d) PC-8.
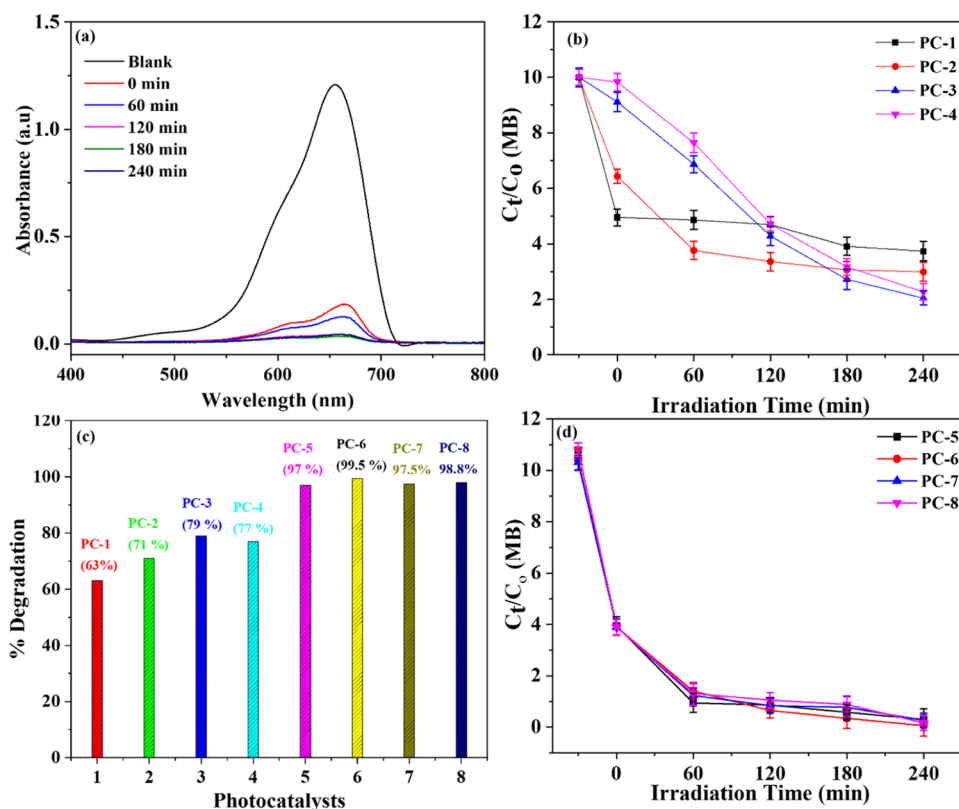
Figure 8. (a) UV−visible spectra of PC-6 for degradation of MB. (b) Concentration of MB with PC-1, PC-2, PC-3, and PC-4 as a function of irradiation time. (c) Photodegradation of MB by all of the catalysts. (d) Variation in MB concentration against irradiation time. (Blank represents MB degradation in the absence of a catalyst). C_t/C_o was calculated using the formula $A_o/C_o = A_t/C_t$, C_o and C_t are the initial concentration and the concentration at a specific time, respectively, while A_o and A_t are the initial absorbance and the absorbance at a specific time, respectively.

indicates the efficient charge/energy transfer between the MOF and incorporated BiOI. In this regard, the drastic PL quenching in PC-6 and PC-8 means that the generated charges from the incorporated BiOI might well transfer to the MOF and then be consumed by the photocatalytic reaction. Finally, PC-6 was chosen for the design-expert BBD-RSM studies because it showed slightly higher photocatalytic activity than the other composites (Figure 8c,d).

RSM was used to statistically analyze the processes, explore their interactions, and optimize the procedures. Three independent variables were analyzed using the BBD model, and their responses are listed in Table 3. The data shown in Table 3 suggests that the quadratic model is the optimal mathematical model; thus, the final equation in terms of the coded factors is as follows

$$\text{dye degradation} = +96.29 - 0.5137A + 0.2838B$$
$$- 0.3725C + 0.0300AB - 0.6775AC$$
$$- 0.9575BC + 0.0175A^2 + 2.40B^2$$
$$- 1.59C^2$$

where A, B, and C represent the concentration, time, and catalyst dosage, respectively. Equations defined in terms of the coded factors can be used to generate predictions regarding the behavior of a specific level of each factor. The factors are usually coded as +1 for higher values and −1 for lower values. The coded equation can also be used to assess the relative significance of variables by comparing the factor coefficients.

Table 3. Actual Experimental Results Obtained through a Box−Behnken Design

run	factor A concentration (ppm)	factor B degradation time (min)	factor C catalyst dosage (g)	experimental response degradation efficiency (%)
1	8	90	0.14	96.50
2	8	120	0.08	98.61
3	10	90	0.2	93.08
4	6	60	0.14	98.90
5	6	90	0.08	95.00
6	8	120	0.2	96.06
7	6	120	0.14	99.50
8	8	90	0.14	96.55
9	8	90	0.14	96.51
10	8	90	0.14	95.95
11	6	90	0.2	95.50
12	10	120	0.14	98.57
13	8	60	0.08	96.22
14	10	90	0.08	95.29
15	8	60	0.2	97.50
16	10	60	0.14	97.85
17	8	90	0.14	96.00

The quadratic model was highly significant according to the analysis of variance (ANOVA).[42]

Table 4 presents the ANOVA results for the quadratic model. P-values, along with Fisher's F-test, were used to confirm the statistical significance of the model, which yielded an F-value of 88.17. The model is considered statistically

Table 4. ANOVA Results for the Quadratic Model

| source	sum of squares	degree of freedom	freedom	F-value	P-value	
model	42.64	9	4.74	88.17	<0.0001	significant
A-conc	2.11	1	2.11	39.30	0.0004	
B-time	0.6441	1	0.6441	11.99	0.0105	
C-catalyst	1.11	1	1.11	20.66	0.0027	
AB	0.0036	1	0.0036	0.0670	0.8032	
AC	1.84	1	1.84	34.17	0.0006	
BC	3.67	1	3.67	68.25	<0.0001	
A^2	0.0013	1	0.0013	0.0240	0.8813	
B^2	24.20	1	24.20	450.42	<0.0001	
C^2	10.64	1	10.64	198.11	<0.0001	
residual	0.3761	7	0.0537			
lack of fit	0.0441	3	0.0147	0.1772	0.9066	insignificant
pure error	0.3320	4	0.0830			
cor total	43.01	16				
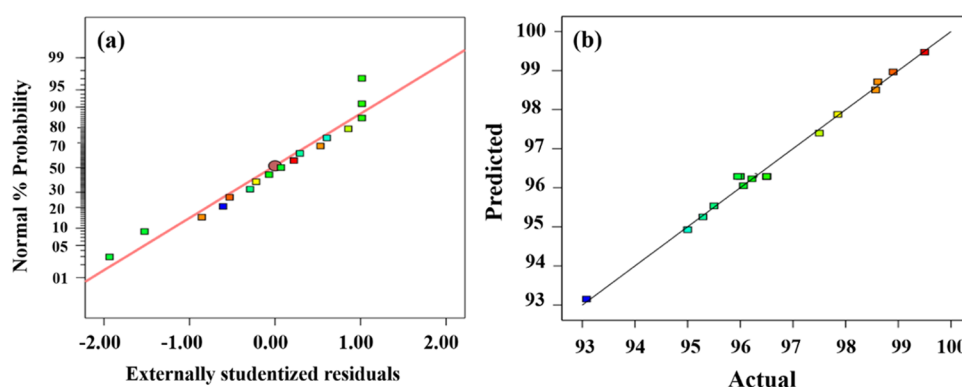
Figure 9. (a) Plot illustrating the normal distribution of linear models depicting the MB degradation efficiency of PC-6. (b) Comparison between observed and predicted results for MB degradation.

Table 5. Regression Analysis of the ANOVA

std. dev.	mean	CV (%)	R^2	adjusted R^2	predicted R^2	adequate precision
0.2318	96.68	0.2398	0.9913	0.9800	0.9715	35.5417

significant when the P value is less than 0.0500.[43] As shown in Table 4, the P-values associated with A, B, C, AC, BC, B^2, and C^2 are less than 0.0500; therefore, these are important model parameters. The acquired F- and P-values indicated that the model was statistically significant. In addition, the lack-of-fit term had an F-value of 0.9066, suggesting that this parameter was not significant compared to the pure error. Nonsignificant lack of fit is desirable, as there is more than 90% chance that a significant lack of fit is the cause of the noise.

The coefficient of regression (R^2), which denotes the correlation between the experimental and predicted data, was used to assess the significance of the model. A plot of the experimental response produced by the model with the expected responses (Figure 9) exhibits a high coefficient of regression $(R^2 = 0.9913)$, indicating the ability of the model to accurately describe the true interactions between the parameters. Parameters derived from the regression analysis of this plot are listed in Table 5. The adjusted R^2 (0.9800) showed that the independent factors accounted for 98% of the total alternation, while 2% of the total alternation was not explained by the model. Similarly, the predicted R^2 value demonstrates the ability of the regression model to predict new observations. The difference between the predicted R^2 of 0.9715 and the adjusted R^2 of 0.9800 was very low (0.0085),

indicating a significant agreement between the predicted and observed responses. Adequate precision evaluates the signal-to-noise ratio, and a ratio exceeding 4 is desirable. In our study, a ratio of 35.542 indicated a statistically significant signal level. Consequently, this model can efficiently guide exploration within the design space.

The residual, which indicated the difference between the experimental and predicted responses, was used to assess the suitability and significance of the model. These residuals can be anticipated, and unexplained variations for a normal distribution may originate from a fitted model.[44] The normality of these residuals can be visually assessed using normal probability plots,[33] which compare the predicted and residual responses (Figure 9a,b). Comparing the experimental and predicted results is crucial in assessing the suitability of the model. To ensure an ideal data distribution, it is important to examine whether the residual values conform to a normal distribution. This assessment helps determine the reliability of the predictive model results.[45] Furthermore, the best fit of the model can be assessed by considering the positions of data points relative to the fitted line. A plot of normal probability against externally studentized residuals (Figure 9a) revealed a linear relationship with some anomalies, suggesting that optimal model performance would be achieved when data
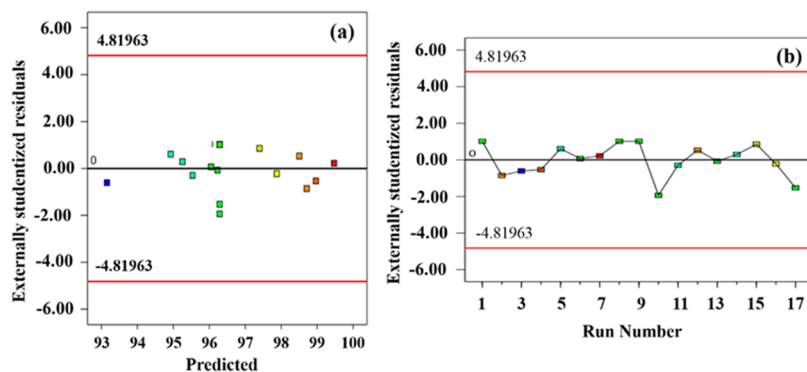
Figure 10. Normal probability plots of residual for the dye removal showing residuals plotted as a function of the (a) predicted response and (b) run number.
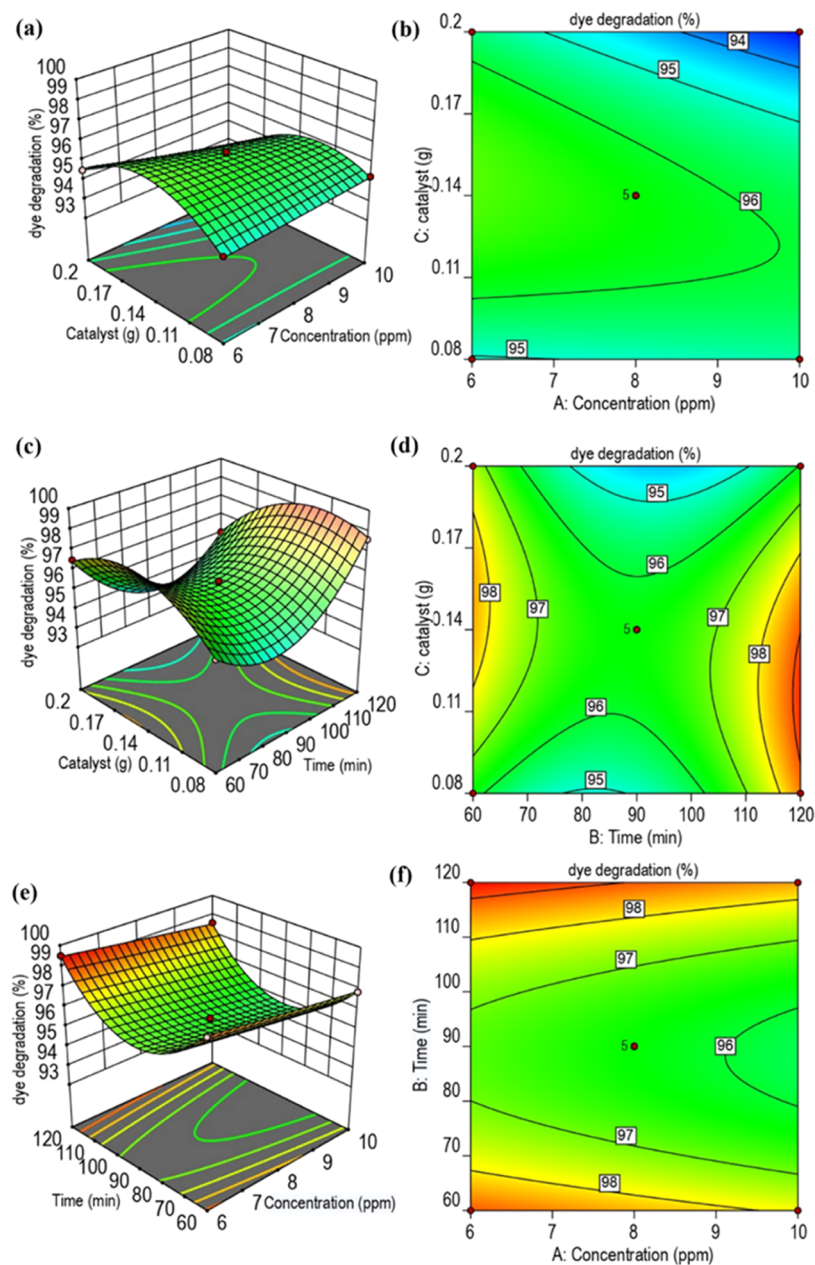

Figure 11. Surface graphs of MB degradation highlighting (a, b) the relationship between the photocatalyst dose and dye concentration with constant irradiation time, (c, d) the relationship between the photocatalyst dose and irradiation time with constant dye concentration, and (e, f) the relationship between irradiation time and dye concentration with constant photocatalyst dose.

Table 6. MOF-Based Photocatalysts for Dye Degradation

MOF photocatalyst	organic dye	irradiation time (min)	removal (%)	references
MOF, $[Cu(4.4'\text{-bipy}) \, Cl]_n + H_2O_2$	MB	150	94.0	47
MOF, $[Co(4.4'\text{-bipy}) \, (HCOO)_2]_n + H_2O_2$	MB	150	55.0	47
$Fe_2O_5/MIL\text{-}53(Fe)$	MB	240	70.0	48
$rGO/NH_2\text{-}MIL\text{-}125$	MB	30	100.0	49
PC-6	MB	120	99.9	this work

points conform to normal distribution conditions. Therefore, the data would exhibit linearity if the connecting line forms a 45° angle.[43] As a result, an assessment of both residuals and the distribution plot (Figure 9b) was conducted to evaluate the appropriateness of the models utilized for depicting the degradation of MB via the Fenton oxidation process.[46] We assessed the adequacy and significance of our model by examining the alignment of the plotted points with the theoretical line of normality (Figure 9b).

Similarly, Figure 10a effectively illustrates the random nature of the residuals with respect to the predicted response, demonstrating that no observable patterns or trends could be observed in the experimental data. This scatter plot shows the absence of systematic variation, confirming the unexpected behavior of the residuals. In addition, a plot of residuals as a function of the run number shows a scattered, random distribution (Figure 10b). These results are significant in determining the adequacy and validity of the model used.[33,43]

3.6. Response Surface Analysis. RSM was employed to create contour plots in two dimensions, focusing on a two-parameter investigation while maintaining the third parameter at a constant value. This analysis aimed to assess the interrelationship among the three factors, catalyst dosage, dye concentration, and irradiation time, which influence MB degradation. Three-dimensional response surface plots were also recorded, which depicted the interface of the MB deterioration while simultaneously considering all three factors. The effects of the amount of photocatalyst, visible light irradiation time, and dye concentration on the rate of MB degradation are demonstrated in Figure 11a−f. Notably, increasing the dye concentration resulted in only a slight increase in MB degradation, suggesting that an optimum dye concentration exists, beyond which no further significant enhancement of MB degradation is obtained. The MB concentration and catalyst dose exhibit a nonlinear relationship (Figure 11a). Dye degradation was markedly improved upon increasing the catalyst dose from 0.08 to 0.14 g; however, a reduction in the degradation rate was observed upon further increasing the catalyst dose from 0.14 to 0.2 g. Similarly, the contour plot shows that the maximum dye degradation rate was obtained with a catalyst dose ranging from 0.13 to 0.14 g and a dye concentration of 9−10 ppm (Figure 11b). These results illustrate that 0.14 g is the optimum catalyst dose, beyond which any further increase in the catalyst has a negative effect on the degradation process, likely owing to the agglomeration of the catalyst. Additionally, these results indicated a direct proportional relationship between the amount of catalyst and the MB concentration.

We further explored the influence of the catalyst dose and visible-light exposure time on the MB degradation rate using three-dimensional response surface and contour plots to visualize and evaluate the effects (Figure 11c,d). The relationship between these two factors was nonlinear, which is consistent with our previous observations. An increase in the

catalyst dose from 0.08 to 0.14 g significantly increased MB degradation; however, a further increase in catalyst dose from 0.14 to 0.2 g led to a reduced degradation rate, further confirming the optimum catalyst dose of 0.14 g. An exposure time of 60−120 min of irradiation was considered because the observed degradation rate exceeded 90% within this span. The degradation rate initially declined between 60 and 80 min of irradiation; however, from 80 to 120 min, the degradation rate considerably increased, with 98% MB degradation after 120 min of exposure to visible light. These results demonstrate the importance of the irradiation time in the degradation process. In agreement with previous observations, the photocatalyst dose and irradiation time showed directly proportional relationships with the MB degradation rate, that is higher degradation rates were achieved by adding more catalyst and extending the irradiation time. Similarly, the effects of the MB concentration and irradiation time are shown in Figure 11e,d. Increasing the concentration of MB from 6 to 10 ppm only slightly increased MB degradation. The exposure time demonstrated an effect similar to that of the catalyst dose.

Table 6 compares the photodegradation of MB in the present work employing PC-6 to that obtained by previous studies.

4. CONCLUSIONS

In this study, we have synthesized and characterized four metal−organic frameworks (MOFs) and their composites with BiOI using two different organic ligands. The potential of these materials as catalysts for the degradation of cationic dyes in industrial effluents was explored. The combination of MOFs with BiOI achieved superior photocatalytic activity for dye removal from aqueous solutions under direct sunlight, surpassing other prepared photocatalysts, particularly in the case of the porous heterostructure Co/Cu-DHTA@BiOI-15% (PC-6). To optimize the process, reduce costs, and improve time efficiency, the Box−Behnken design of the response surface methodology (RSM) was used, which allowed the relationship between three parameters, namely, the initial dye concentration (6−10 ppm), catalyst dosage (0.08−0.2 g L^{-1}), and irradiation time (60−120 min), to be elucidated with just 17 experiments. By employing the BBD design, we determined the optimal conditions for dye degradation, which included an initial dye concentration of 6 ppm, a catalyst dosage of 0.14 g L^{-1}, and an irradiation time of 120 min. BBD-RSM analysis predicted a coefficient of regression (R^2) of 0.97 for dye removal, while the experimental R^2 obtained under optimal conditions was 0.98. ANOVA validated the accuracy and reliability of the model, with a significant F-value (88.17), P-value (<0.0001), appropriate precision (35.54), and a non-significant lack of fit. Furthermore, the 3D plot derived from the BBD-RSM indicated that the optimal interaction occurred at the middle of the range of examined dye concentrations. Notably, the maximum photocatalytic degradation of MB was achieved with relatively low catalyst concentrations. Our

findings highlight the potential of synthesized heterostructures using in situ methods as highly effective photocatalysts for the degradation of organic contaminants, supported by the BBD-RSM design approach. This study provides valuable insights into the development of efficient and cost-effective photocatalytic materials for environmental remediation. For example, adjusting the metal ions and combination ratio to various ligands and heteroatoms in the MOF system can further modify the photoactivity and intrinsic band gaps, expanding them to the various photoinduced electrochemical applications.[50−53]

■ ASSOCIATED CONTENT

Ⓢ Supporting Information

The Supporting Information is available free of charge at https://pubs.acs.org/doi/10.1021/acsestwater.3c00667.

UV−visible spectra of all of the prepared photocatalysts (PDF)

■ AUTHOR INFORMATION

Corresponding Authors

Toheed Akhter − *Department of Chemistry, School of Science, University of Management and Technology, 54770 Lahore, Pakistan;* ⓘ orcid.org/0000-0003-3852-0485; Email: toheed.akhter@umt.edu.pk

Chan Ho Park − *Department of Chemical and Biological Engineering, Gachon University, Seongnam 13120, Korea;* ⓘ orcid.org/0000-0002-1832-4842; Email: chhopark@gachon.ac.kr

Authors

Iqra Afzal − *Department of Chemistry, School of Science, University of Management and Technology, 54770 Lahore, Pakistan*

Sadaf Ul Hassan − *Department of Chemistry, COMSATS University Islamabad, Lahore 54000, Pakistan*

Ho Kyung Lee − *Department of Chemical and Biological Engineering, Gachon University, Seongnam 13120, Korea*

Shumaila Razzaque − *Institute of Physical Chemistry, Polish Academy of Sciences, 01-224 Warsazawa, Poland*

Asif Mahmood − *Department of Chemical Engineering, College of Engineering, King Saud University, Riyadh 11421, Saudi Arabia*

Waheed Al-Masry − *Department of Chemical Engineering, College of Engineering, King Saud University, Riyadh 11421, Saudi Arabia;* ⓘ orcid.org/0000-0003-4379-8895

Hansol Lee − *Department of Chemical and Biological Engineering, Gachon University, Seongnam 13120, Korea*

Complete contact information is available at:
https://pubs.acs.org/10.1021/acsestwater.3c00667

Author Contributions

Conceptualization: I.A. and T.A.; methodology: I.A., T.A., S.U.H.; validation: T.A. and S.U.H.; formal analysis: I.A.; investigation: I.A.; resources: S.R., A.M., W.A.-M.; writing—original draft preparation: I.A. and T.A.; writing—review and editing: H.K.L., H.L., C.H.P.; supervision: T.A.; all authors have read and agreed to the published version of the manuscript. CRediT: **Iqra Afzal** conceptualization, formal analysis, investigation, methodology, writing-original draft; **Toheed Akhter** conceptualization, methodology, supervision, validation, writing-original draft; **Sadaf Ul Hassan** methodology, validation; **Ho Kyung Lee** writing-review & editing; **Shumaila Razzaque** resources; **Asif Mahmood** resources; **Waheed Al-Masry** resources; **Hansol Lee** writing-review & editing; **Chan Ho Park** writing-review & editing.

Notes

The authors declare no competing financial interest.

■ ACKNOWLEDGMENTS

■ REFERENCES

(1) Zhang, W.; Liu, D.; Mu, Z.; Zhang, X.; Dong, G.; Bai, L.; Guo, R.; Li, J.; Zhao, M.; Zhang, Z. Insight into the Novel Z-scheme ZIF67/WO$_3$ Heterostructure for Improved Photocatalytic Degradation of Methylene Blue under visible light. *J. Inorg. Organomet. Polym. Mater.* **2023**, *33* (1), 90−104.

(2) Kalaiarasi, K.; Lavanya, A.; Amsamani, S.; Bagyalakshmi, G. Decolourization of textile dye effluent by non-viable biomass of Aspergillus fumigatus. *Braz. Arch. Biol. Technol.* **2012**, *55*, 471−476.

(3) Peydayesh, M.; Suter, M. K.; Bolisetty, S.; Boulos, S.; Handschin, S.; Nyström, L.; Mezzenga, R. Amyloid fibrils aerogel for sustainable removal of organic contaminants from water. *Adv. Mater.* **2020**, *32* (12), No. 1907932, DOI: 10.1002/adma.201907932.

(4) Kaith, B.; Sharma, J.; Sukriti; Sethi, S.; Kaur, T.; Shanker, U.; Jassal, V. Fabrication of green device for efficient capture of toxic methylene blue from industrial effluent based on K$_2$Zn$_3$ [Fe (CN) 6]$_2$· 9H$_2$O nanoparticles reinforced gum xanthan-psyllium hydrogel nanocomposite. *J. Chin. Adv. Mater. Soc.* **2016**, *4* (4), 249−268.

(5) Bhatnagar, A.; Sillanpää, M.; Witek-Krowiak, A. Agricultural waste peels as versatile biomass for water purification−A review. *Chem. Eng. J.* **2015**, *270*, 244−271.

(6) Lau, Y.-Y.; Wong, Y.-S.; Teng, T.-T.; Morad, N.; Rafatullah, M.; Ong, S.-A. Degradation of cationic and anionic dyes in coagulation−flocculation process using bi-functionalized silica hybrid with aluminum-ferric as auxiliary agent. *RSC Adv.* **2015**, *5* (43), 34206−34215.

(7) Saffaj, N.; Loukili, H.; Younssi, S. A.; Albizane, A.; Bouhria, M.; Persin, M.; Larbot, A. Filtration of solution containing heavy metals and dyes by means of ultrafiltration membranes deposited on support made of Moroccan clay. *Desalination* **2004**, *168*, 301−306.

(8) Zhang, J.; Lee, K.-H.; Cui, L.; Jeong, T.-s. Degradation of methylene blue in aqueous solution by ozone-based processes. *J. Ind. Eng. Chem.* **2009**, *15* (2), 185−189.

(9) Kumar, S.; Ojha, A. K. Oxygen vacancy induced photoluminescence properties and enhanced photocatalytic activity of ferromagnetic ZrO$_2$ nanostructures on methylene blue dye under ultra-violet radiation. *J. Alloys Compd.* **2015**, *644*, 654−662.

(10) Aroguz, A. Z.; Gulen, J.; Evers, R. Adsorption of methylene blue from aqueous solution on pyrolyzed petrified sediment. *Bioresour. Technol.* **2008**, *99* (6), 1503−1508.

(11) Pinto, F.; Wilson, A.; Moss, B.; Kafizas, A. Systematic Exploration of WO$_3$/TiO$_2$ Heterojunction Phase Space for Applications in Photoelectrochemical Water Splitting. *J. Phys. Chem. C* **2022**, *126* (2), 871−884.

(12) Jantawasu, P.; Sreethawong, T.; Chavadej, S. Photocatalytic activity of nanocrystalline mesoporous-assembled TiO$_2$ photocatalyst for degradation of methyl orange monoazo dye in aqueous wastewater. *Chem. Eng. J.* **2009**, *155* (1−2), 223−233.

(13) (a) Liang, L.; Chang, Q.; Cai, T.; Li, N.; Xue, C.; Yang, J.; Hu, S. Combining carbon dots with WO3-x nanodots for utilizing the full spectrum of solar radiation in photocatalysis. *Chem. Eng. J.* **2022**, *428*,

No. 131139. (b) Liang, Z.; Yan, C.-F.; Rtimi, S.; Bandara, J. Piezoelectric materials for catalytic/photocatalytic removal of pollutants: Recent advances and outlook. *Appl. Catal., B* **2019**, *241*, 256−269.

(14) (a) Mohabansi, N.; Patil, V.; Yenkie, N. A comparative study on photo degradation of methylene blue dye effluent by advanced oxidation process by using TiO₂/ZnO photo catalyst. *Rasayan J. Chem.* **2011**, *4* (4), 814−819. (b) Khaki, M. R. D.; Shafeeyan, M. S.; Raman, A. A. A.; Daud, W. M. A. W. Application of doped photocatalysts for organic pollutant degradation-A review. *J. Environ. Manage.* **2017**, *198*, 78−94.

(15) Shi, C.; Zhou, X.; Liu, D.; Li, L.; Xu, M.; Sakiyama, H.; Muddassir, M.; Wang, J. A new 3D high connection Cu-based MOF introducing a flexible tetracarboxylic acid linker: Photocatalytic dye degradation. *Polyhedron* **2021**, *208*, No. 115441.

(16) Yang, Y.; Zhang, C.; Lai, C.; Zeng, G.; Huang, D.; Cheng, M.; Wang, J.; Chen, F.; Zhou, C.; Xiong, W. BiOX (X = Cl, Br, I) photocatalytic nanomaterials: applications for fuels and environmental management. *Adv. Colloid Interface Sci.* **2018**, *254*, 76−93.

(17) Wang, H.; Liang, Y.; Liu, L.; Hu, J.; Wu, P.; Cui, W. Enriched photoelectrocatalytic degradation and photoelectric performance of BiOI photoelectrode by coupling rGO. *Appl. Catal., B* **2017**, *208*, 22−34.

(18) Zhang, C.; Fei, W.; Wang, H.; Li, N.; Chen, D.; Xu, Q.; Li, H.; He, J.; Lu, J. pn Heterojunction of BiOI/ZnO nanorod arrays for piezo-photocatalytic degradation of bisphenol A in water. *J. Hazard. Mater.* **2020**, *399*, No. 123109.

(19) Gao, S.; Guo, C.; Lv, J.; Wang, Q.; Zhang, Y.; Hou, S.; Gao, J.; Xu, J. A novel 3D hollow magnetic Fe₃O₄/BiOI heterojunction with enhanced photocatalytic performance for bisphenol A degradation. *Chem. Eng. J.* **2017**, *307*, 1055−1065.

(20) Luo, S.; Tang, C.; Huang, Z.; Liu, C.; Chen, J.; Fang, M. Effect of different Bi/Ti molar ratios on visible-light photocatalytic activity of BiOI/TiO₂ heterostructured nanofibers. *Ceram. Int.* **2016**, *42* (14), 15780−15786.

(21) Liu, K.; Deng, L.; Li, H.; Bao, Y.; Xiao, Z.; Li, B.; Zhou, Q.; Geng, Y.; Wang, L. Two isostructural Co/Ni fluorine-containing metal-organic frameworks for dye adsorption and supercapacitor. *J. Solid State Chem.* **2019**, *275*, 1−7.

(22) Masoomi, M. Y.; Morsali, A.; Dhakshinamoorthy, A.; Garcia, H. Mixed-metal MOFs: unique opportunities in metal−organic framework (MOF) functionality and design. *Angew. Chem.* **2019**, *131* (43), 15330−15347.

(23) Ye, G.; Luo, P.; Zhao, Y.; Qiu, G.; Hu, Y.; Preis, S.; Wei, C. Three-dimensional Co/Ni bimetallic organic frameworks for high-efficient catalytic ozonation of atrazine: Mechanism, effect parameters, and degradation pathways analysis. *Chemosphere* **2020**, *253*, No. 126767.

(24) Wu, Q.; Siddique, M. S.; Yu, W. Iron-nickel bimetallic metal-organic frameworks as bifunctional Fenton-like catalysts for enhanced adsorption and degradation of organic contaminants under visible light: Kinetics and mechanistic studies. *J. Hazard. Mater.* **2021**, *401*, No. 123261.

(25) Chu, D.; Li, F.; Song, X.; Ma, H.; Tan, L.; Pang, H.; Wang, X.; Guo, D.; Xiao, B. A novel dual-tasking hollow cube NiFe₂O₄-NiCo-LDH@rGO hierarchical material for high preformance supercapacitor and glucose sensor. *J. Colloid Interface Sci.* **2020**, *568*, 130−138.

(26) Sun, D.; Sun, F.; Deng, X.; Li, Z. Mixed-Metal Strategy on Metal−Organic Frameworks (MOFs) for Functionalities Expansion: Co Substitution Induces Aerobic Oxidation of Cyclohexene over Inactive Ni-MOF-74. *Inorg. Chem.* **2015**, *54* (17), 8639−8643.

(27) Llabrés i Xamena, F. X.; Corma, A.; Garcia, H. Applications for Metal−Organic Frameworks (MOFs) as Quantum Dot Semiconductors. *J. Phys. Chem. C* **2007**, *111* (1), 80−85.

(28) Mahata, P.; Madras, G.; Natarajan, S. Novel Photocatalysts for the Decomposition of Organic Dyes Based on Metal-Organic Framework Compounds. *J. Phys. Chem. B* **2006**, *110* (28), 13759−13768.

(29) Jing, H.-P.; Wang, C.-C.; Zhang, Y.-W.; Wang, P.; Li, R. Photocatalytic degradation of methylene blue in ZIF-8. *RSC Adv.* **2014**, *4* (97), 54454−54462.

(30) Chen, L.; Ren, X.; Alharbi, N. S.; Chen, C. Fabrication of a novel Co/Ni-MOFs@ BiOI composite with boosting photocatalytic degradation of methylene blue under visible light. *J. Environ. Chem. Eng.* **2021**, *9* (5), No. 106194.

(31) (a) Niu, J.; Dai, P.; Zhang, Q.; Yao, B.; Yu, X. Microwave-assisted solvothermal synthesis of novel hierarchical BiOI/rGO composites for efficient photocatalytic degardation of organic pollutants. *Appl. Surf. Sci.* **2018**, *430*, 165−175. (b) Liang, J.; Li, X.; Zuo, J.; Lin, J.; Liu, Z. Hybrid 0D/2D heterostructures: in-situ growth of 0D g-C₃N₄ on 2D BiOI for efficient photocatalyst. *Adv. Compos. Hybrid Mater.* **2021**, *4*, 1122−1136.

(32) Siddiqa, A.; Akhter, T.; Faheem, M.; Razzaque, S.; Mahmood, A.; Al-Masry, W.; Nadeem, S.; Hassan, S. U.; Yang, H.; Park, C. H. Bismuth-Rich Co/Ni Bimetallic Metal−Organic Frameworks as Photocatalysts toward Efficient Removal of Organic Contaminants under Environmental Conditions. *Micromachines* **2023**, *14* (5), 899.

(33) Gholipoor, O.; Hosseini, S. A. Phenol removal from wastewater by CWPO process over the Cu-MOF nanocatalyst: process modeling by response surface methodology (RSM) and kinetic and isothermal studies. *New J. Chem.* **2021**, *45* (5), 2536−2549.

(34) Jensen, W. A. Response surface methodology: process and product optimization using designed experiments. *J. Quality Technol.* **2017**, *49* (2), 186.

(35) Sanz, R.; Martínez, F.; Orcajo, G.; Wojtas, L.; Briones, D. Synthesis of a honeycomb-like Cu-based metal−organic framework and its carbon dioxide adsorption behaviour. *Dalton Trans.* **2013**, *42* (7), 2392−2398.

(36) Mishra, A.; Panigrahi, A.; Mal, P.; Penta, S.; Padmaja, G.; Bera, G.; Das, P.; Rambabu, P.; Turpu, G. R. Rapid photodegradation of methylene blue dye by rGO-V₂O₅ nano composite. *J. Alloys Compd.* **2020**, *842*, No. 155746.

(37) Doan, V. D.; Do, T. L.; Ho, T. M. T.; Le, V. T.; Nguyen, H. T. Utilization of waste plastic pet bottles to prepare copper-1, 4-benzenedicarboxylate metal-organic framework for methylene blue removal. *Sep. Sci. Technol.* **2020**, *55* (3), 444−455.

(38) Zha, Q.; Li, M.; Liu, Z.; Ni, Y. Hierarchical Co,Fe-MOF-74/Co/Carbon Cloth Hybrid Electrode: Simple Construction and Enhanced Catalytic Performance in Full Water Splitting. *ACS Sustainable Chem. Eng.* **2020**, *8* (32), 12025−12035.

(39) Bagheri, A. R.; Ghaedi, M. Magnetic metal organic framework for pre-concentration of ampicillin from cow milk samples. *J. Pharm. Anal.* **2020**, *10* (4), 365−375.

(40) Kaur, R.; Kaur, A.; Umar, A.; Anderson, W. A.; Kansal, S. K. Metal organic framework (MOF) porous octahedral nanocrystals of Cu-BTC: Synthesis, properties and enhanced adsorption properties. *Mater. Res. Bull.* **2019**, *109*, 124−133.

(41) Zheng, W.; Feng, S.; Shao, C.; Zhu, G.; Ni, Z.; Sun, J.; Huang, X. Visible light-driven BiOI/ZIF-8 heterostructure and photocatalytic adsorption synergistic degradation of BPA. *Res. Chem. Intermed.* **2020**, *46*, 2951−2967.

(42) Dastkhoon, M.; Ghaedi, M.; Asfaram, A.; Goudarzi, A.; Mohammadi, S. M.; Wang, S. Improved adsorption performance of nanostructured composite by ultrasonic wave: Optimization through response surface methodology, isotherm and kinetic studies. *Ultrason. Sonochem.* **2017**, *37*, 94−105.

(43) Hassan, S. U.; Shafique, S.; Palvasha, B. A.; Saeed, M. H.; Naqvi, S. A. R.; Nadeem, S.; Irfan, S.; Akhter, T.; Khan, A. L.; Nazir, M. S. Photocatalytic degradation of industrial dye using hybrid filler impregnated poly-sulfone membrane and optimizing the catalytic performance using Box-Behnken design. *Chemosphere* **2023**, *313*, No. 137418. DOI: 10.1016/j.chemosphere.2022.137418.

(44) (a) Majdi, H.; Esfahani, J. A.; Mohebbi, M. Optimization of convective drying by response surface methodology. *Comput. Electron. Agric.* **2019**, *156*, 574−584. (b) Danmaliki, G. I.; Saleh, T. A.; Shamsuddeen, A. A. Response surface methodology optimization of

adsorptive desulfurization on nickel/activated carbon. *Chem. Eng. J.* **2017**, *313*, 993−1003.

(45) (a) Vebber, M. C.; da Silva Crespo, J.; Giovanela, M. Self-assembled thin films of PAA/PAH/TiO₂ for the photooxidation of ibuprofen. Part I: Optimization of photoactivity using design of experiments and surface response methodology. *Chem. Eng. J.* **2019**, *360*, 1447−1458. (b) Mortazavian, S.; Saber, A.; James, D. E. Optimization of photocatalytic degradation of acid blue 113 and acid red 88 textile dyes in a UV-C/TiO₂ suspension system: application of response surface methodology (RSM). *Catalysts* **2019**, *9* (4), 360.

(46) Du, J.-J.; Yuan, Y.-P.; Sun, J.-X.; Peng, F.-M.; Jiang, X.; Qiu, L.-G.; Xie, A.-J.; Shen, Y.-H.; Zhu, J.-F. New photocatalysts based on MIL-53 metal−organic frameworks for the decolorization of methylene blue dye. *J. Hazard. Mater.* **2011**, *190* (1−3), 945−951.

(47) Zhang, M.; Wang, L.; Zeng, T.; Shang, Q.; Zhou, H.; Pan, Z.; Cheng, Q. Two pure MOF-photocatalysts readily prepared for the degradation of methylene blue dye under visible light. *Dalton Trans.* **2018**, *47* (12), 4251−4258.

(48) Feng, X.; Chen, H.; Jiang, F. In-situ ethylenediamine-assisted synthesis of a magnetic iron-based metal-organic framework MIL-53 (Fe) for visible light photocatalysis. *J. Colloid Interface Sci.* **2017**, *494*, 32−37.

(49) Huang, L.; Liu, B. Synthesis of a novel and stable reduced graphene oxide/MOF hybrid nanocomposite and photocatalytic performance for the degradation of dyes. *RSC Adv.* **2016**, *6* (22), 17873−17879.

(50) Wang, M.; Wang, J.; Xi, C.; Cheng, C.; Zou, C.; Zhang, R.; Xie, Y.; Guo, Z.; Tang, C.; Dong, C.; Chen, Y.; Du, X. Hydrogen-Deficient Nickel−Cobalt Double Hydroxide for Photocatalytic Overall Water Splitting. *Angew. Chem., Int Ed.* **2020**, *59* (28), 11510−11515.

(51) Li, S.; Shang, H.; Tao, Y.; Li, P.; Pan, H.; Wang, Q.; Zhang, S.; Jia, H.; Zhang, H.; Cao, J.; Zhang, B.; Zhang, R.; Li, G.; Zhang, Y.; Zhang, D.; Li, H. Hydroxyl Radical-Mediated Efficient Photo-electrocatalytic NO Oxidation with Simultaneous Nitrate Storage Using A Flow Photoanode Reactor. *Angew. Chem., Int Ed.* **2023**, *62* (28), No. e202305538. DOI: 10.1002/anie.202305538.

(52) Jiang, Y.; Li, S.; Wang, S.; Zhang, Y.; Long, C.; Xie, J.; Fan, X.; Zhao, W.; Xu, P.; Fan, Y.; Cui, C.; Tang, Z. Enabling Specific Photocatalytic Methane Oxidation by Controlling Free Radical Type. *J. Am. Chem. Soc.* **2023**, *145* (4), 2698−2707.

(53) Wang, S.; Guan, B. Y.; Lou, X. W. D. Construction of ZnIn₂S₄−In₂O₃ Hierarchical Tubular Heterostructures for Efficient CO₂ Photoreduction. *J. Am. Chem. Soc.* **2018**, *140* (15), 5037−5040.

📖 Recommended by ACS

A Novel 2D Copper–Organic Framework for Catalyzing CO₂ Chemical Fixation and Luminescence Sensing

Yuanhang Zhang, Bin Zhao, *et al.*

OCTOBER 19, 2023

CRYSTAL GROWTH & DESIGN   READ 🗗

Selective Integrating Molecular Catalytic Units into Bipyridine-Based Covalent Organic Frameworks for Specific Photocatalytic Fuel Production

Dengmeng Song, Ning Wang, *et al.*

FEBRUARY 08, 2024

INORGANIC CHEMISTRY   READ 🗗

Dual-Ligand Strategy for the Design and Construction of a Cd–Zn Heterometallic Metal–Organic Framework by One-Pot Synthesis as a Heterogeneous Catalyst for the Epoxida...

Akram Karbalaee Hosseini, Barzin Safarkoopayeh, *et al.*

DECEMBER 14, 2023

INORGANIC CHEMISTRY   READ 🗗

Schiff Base Complex Cocatalyst with Coordinatively Unsaturated Cobalt Sites for Photoelectrochemical Water Oxidation

Yangpei Li, Yougui Li, *et al.*

OCTOBER 18, 2023

INORGANIC CHEMISTRY   READ 🗗

Get More Suggestions >